Observational evidence that cloud feedback amplifies global warming

Paulo Ceppi[a,1,2] **and Peer Nowack**[a,b,c,1]

[a]Grantham Institute and Department of Physics, Imperial College London, London SW7 2AZ, UK; [b]Data Science Institute, Imperial College London, London SW7 2AZ, UK; [c]Climatic Research Unit, School of Environmental Sciences, University of East Anglia, Norwich NR4 7TJ, UK

This manuscript was compiled on June 14, 2021

Global warming drives changes in Earth's cloud cover, which in turn have the potential to strongly amplify or dampen climate change. This 'cloud feedback' is the single most important cause of uncertainty in Equilibrium Climate Sensitivity (ECS) – the equilibrium global warming following a doubling of atmospheric carbon dioxide. Using data from Earth observations and climate model simulations, we here develop a novel statistical learning analysis of how clouds respond to changes in the environment. We show that global cloud feedback is dominated by the sensitivity of clouds to surface temperature and tropospheric stability. Considering changes in just these two factors, we are able to constrain global cloud feedback to 0.43 ± 0.35 W m^{-2} K^{-1} (90% confidence), implying a robustly amplifying effect of clouds on global warming and only a 0.5% chance of ECS below 2 K. We thus anticipate that our new approach will enable tighter constraints on climate change projections, including its manifold socioeconomic and ecological impacts.

Climate change | Clouds | Climate feedbacks | Climate modeling | Climate sensitivity

Clouds have long been recognized as the leading source of uncertainty in Earth's climate response to anthropogenic forcing through their key role in modulating the global energy balance. While a combined assessment of all available lines of evidence – theory, modeling and Earth observations – suggests that cloud feedback is likely positive, i.e. amplifies global warming (1–3), so far a narrow constraint on this feedback has remained elusive. This is reflected in the broad 90% confidence interval for cloud feedback (-0.09 to $+0.99$ W m^{-2} K^{-1}) estimated in a recent assessment under the auspices of the World Climate Research Programme (WCRP; 3), which relied both on a review of existing studies and expert judgment. Part of the challenge stems from the variety of physical processes contributing to the net cloud feedback, involving the interaction of clouds with both solar (shortwave) and terrestrial (longwave) radiative fluxes (4).

Uncertainty in cloud feedback has persisted because each line of evidence comes with its limitations and challenges. Theory cannot provide precise projections. Global climate models (GCMs) are unable to explicitly represent small-scale cloud processes on their coarse spatial grids, resulting in large spread in their simulation of cloud feedback (4, 5). High-resolution models may better represent such cloud processes, but limitations in computational power prevent climate change experiments on global grids (6). Most of the available observational estimates of cloud feedback are restricted to particular regions and circulation regimes such as tropical subsidence regions (7–11) or extratropical mixed-phase clouds (12, 13), and are uncertain owing to the short satellite record of global cloud-radiative measurements and the numerous, co-varying meteorological factors controlling clouds.

Statistical learning framework. Here we develop a novel statistical learning analysis to calculate an observational constraint on global cloud feedback that significantly improves on previous estimates and does not require high-resolution simulations or observations. The method is based on cloud-controlling factor analysis (7, 8, 10, 11, 14–16), where we assume that cloud-radiative anomalies at grid point r, $\mathrm{d}C(r)$, can be approximated as a linear function of anomalies in a set of M relevant meteorological cloud-controlling factors $\mathrm{d}\boldsymbol{X}_i(r)$:

$$\mathrm{d}C(r) \approx \sum_{i=1}^{M} \frac{\partial C(r)}{\partial \boldsymbol{X}_i(r)} \cdot \mathrm{d}\boldsymbol{X}_i(r) = \sum_{i=1}^{M} \boldsymbol{\Theta}_i(r) \cdot \mathrm{d}\boldsymbol{X}_i(r). \quad [1]$$

$\boldsymbol{\Theta}_i(r)$ represents the *sensitivities* of $C(r)$ to the controlling factors. As a key difference to previous studies (7, 8, 10, 11, 14) focused on grid-point-wise relationships, e.g. between surface temperature at point r and $C(r)$, we here model cloud-radiative anomalies at grid point r as a function of the controlling factor variables within a $105^\circ \times 55^\circ$ (longitude $\times$ latitude) domain centered on r (see Figs. 1 and S1 for an example). The contribution of each controlling factor to $\mathrm{d}C(r)$ is then obtained by the scalar product of the spatial vectors $\boldsymbol{\Theta}_i(r)$ and $\mathrm{d}\boldsymbol{X}_i(r)$.

Different from previous work, we use ridge regression (17) to avoid overfitting when including this large number of predictors in the regressions (Materials and Methods). Importantly, this statistical learning approach allows us to robustly estimate sensitivities $\boldsymbol{\Theta}_i(r)$ despite the presence of many collinear predictors and the limited sample size available from the short

Significance Statement

A key challenge of our time is to accurately estimate future global warming in response to a given increase in atmospheric carbon dioxide – a number known as the *climate sensitivity*. This number is highly uncertain, mainly because it remains unclear how clouds will change with warming. Such changes in clouds could strongly amplify or dampen global warming, providing a climate feedback. Here we perform a novel statistical learning analysis that provides a global observational constraint on the future cloud response. This constraint supports that cloud feedback will amplify global warming, making it very unlikely that climate sensitivity is smaller than 2°C.

The authors collaboratively designed the study, performed the analysis, and wrote the manuscript. P.N. performed the statistical learning calculations, while P.C. performed the calculation of feedback coefficients, created the figures, and wrote the initial draft of the manuscript. Both authors contributed to the interpretation of the results and refinement of the manuscript.

The authors declare no competing interests.

[1]P.C. and P.N. contributed equally to this work.

[2]To whom correspondence should be addressed. E-mail: p.ceppi@imperial.ac.uk

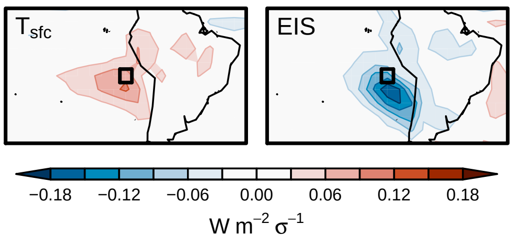

Fig. 1. CMIP mean shortwave cloud-radiative sensitivities to surface temperature, $\boldsymbol{\Theta}_{T_{\mathrm{sfc}}}$, and estimated inversion strength, $\boldsymbol{\Theta}_{\mathrm{EIS}}$ (Eq. 1) for a sample $5^\circ \times 5^\circ$ target grid box in the Southeast Pacific (82.5° W, 17.5° S; black box). Radiative anomalies are normalized for a one–standard deviation (σ) anomaly in the controlling factors, based on monthly variability. See Fig. S1 for the remaining three controlling factors.

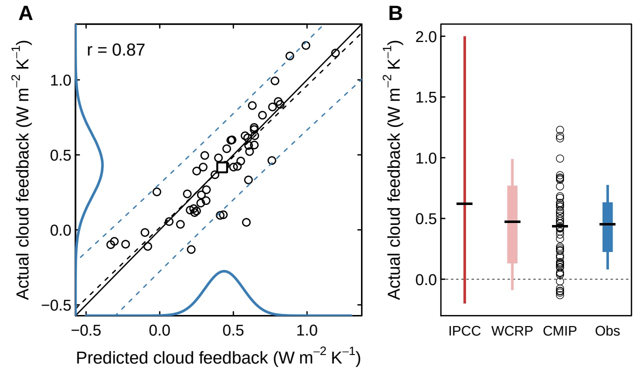

Fig. 2. (A) Actual vs. predicted global-mean cloud feedback for 52 CMIP models (circles) and the multi-model mean (square). The one-to-one line is shown in solid black. Dashed lines represent the least-squares fit (black) and the 5–95% prediction intervals (blue). Blue curves represent probability distributions for the observational estimates (amplitudes scaled arbitrarily). (B) Ranges of cloud feedback values for the IPCC AR5, the WCRP assessment, the CMIP models, and the new observational constraint. Thin and thick bars denote 90% and 66% confidence intervals, respectively. Black horizontal bars indicate the medians for the IPCC, WCRP and observational estimates, and the mean for the CMIP models. No 66% interval was provided for the IPCC cloud feedback estimate.

record of satellite observations (18–20).

We include five controlling factors $\boldsymbol{X}_i$ quantifying surface temperature, estimated boundary-layer inversion strength (21, 22), lower- and upper-tropospheric relative humidity, and mid-tropospheric vertical velocity (see Materials and Methods and Supporting Information). Each regression thus yields five spatial maps of sensitivities at each point r, $\boldsymbol{\Theta}_i(r)$ (Figs. 1 and S1). To estimate these sensitivities from GCMs and observations, we apply ridge regression to monthly $5^\circ \times 5^\circ$ gridded data covering the period March 2000 – September 2019. For models, we use data of 52 GCMs from the Coupled Model Intercomparison Project phases 5 and 6 (CMIP5/6; 23, 24), while for observations we use global satellite cloud-radiative data combined with four reanalysis datasets of meteorological variables (Materials and Methods). For each GCM and observational dataset, we apply separate ridge regressions at each grid point r for longwave or shortwave cloud-radiative anomalies $C(r)$.

As an innovation relative to previous analyses based on purely local predictors, our approach allows us to learn how cloud-radiative variability depends on spatial patterns of cloud-controlling factors – a central advance given that cloud formation is part of a large-scale coupled system (25, 26). Another advantage of our approach is that non-local predictors should be less impacted by the local cloud-radiative feedback on T_{sfc}, which can otherwise lead to biases in the estimation of the sensitivity to surface temperature (27).

Prediction model. Once the sensitivities have been estimated, we predict the local cloud feedback $\lambda_C(r)$ using only the two controlling factors surface temperature (T_{sfc}) and estimated inversion strength (EIS; Materials and Methods):

$$\lambda_C(r) = \frac{\mathrm{d}C(r)}{\mathrm{d}T} \approx \boldsymbol{\Theta}_{T_{\mathrm{sfc}}}(r) \cdot \frac{\mathrm{d}\boldsymbol{T}_{\mathbf{sfc}}(r)}{\mathrm{d}T} + \boldsymbol{\Theta}_{\mathrm{EIS}}(r) \cdot \frac{\mathrm{d}\mathbf{EIS}(r)}{\mathrm{d}T}, \quad [2]$$

where the controlling factor responses per unit global warming, $\mathrm{d}\boldsymbol{T}_{\mathbf{sfc}}(r)/\mathrm{d}T$ and $\mathrm{d}\mathbf{EIS}(r)/\mathrm{d}T$, are estimated for each GCM from an integration with step-like CO_2 forcing (Fig. S2A–B; Materials and Methods). Prior work has shown that surface temperature and stability account for most of the forced response of marine low clouds (7, 8), and jointly explain a large fraction of forced and unforced variability in the global radiative budget (28). Here we will demonstrate that these two factors also explain most of the inter-model spread in global cloud feedback. By using only controlling factors related to temperature, we keep our prediction model as simple as possible and ensure to include only factors that are external to the clouds. Accounting for additional factors at the regression training stage in Eq. 1 only serves to ensure that the cloud sensitivities to T_{sfc} and EIS are accurately estimated, conditional on fixed humidity and vertical velocity – a necessary step given that these environmental factors strongly covary on monthly timescales. The sensitivity of our results to the inclusion of additional predictors in Eq. 2, or to a change in the size of the regional domain used in the ridge regressions, is discussed in the Supporting Information.

An observational constraint on cloud feedback. Underlying Eq. 2 is the assumption that the sensitivities learned from present-day climate according to Eq. 1 are time-scale invariant, i.e. that they describe both monthly unforced cloud-radiative responses to T_{sfc} and EIS and long-term cloud feedbacks (11). To validate this assumption, we use GCMs to compare the cloud feedbacks predicted using Eq. 2 to the actual values derived from abrupt-4xCO2 simulations (Materials and Methods). To achieve this, we make a prediction for each GCM by multiplying the model-specific sensitivities and controlling factor responses (Eq. 2), adding up the local longwave and shortwave components, and taking the area-weighted mean. We find that these predictions are in excellent agreement with the actual GCM cloud feedbacks ($r = 0.87$ across the 52 CMIP models; Fig. 2A, black circles), closely following a one-to-one relationship. We highlight that this result has been achieved using just under 20 years of monthly GCM data in each case (equivalent to the length of the satellite record) to learn the cloud-controlling sensitivities. The method has skill for both the longwave and shortwave components of the feedback (Fig. S3A–B); we obtain a higher correlation for the shortwave feedback ($r_{\mathrm{SW}} = 0.87$ vs $r_{\mathrm{LW}} = 0.68$), which dominates the overall model spread.

We can then obtain an observational constraint on cloud feedback by substituting observed estimates of $\boldsymbol{\Theta}_{T_{\mathrm{sfc}}}$ and $\boldsymbol{\Theta}_{\mathrm{EIS}}$ into Eq. 2. While we do not constrain the CO_2-driven

$\mathrm{d}\boldsymbol{T}_{\mathbf{sfc}}/\mathrm{d}T$ and $\mathrm{d}\mathbf{EIS}/\mathrm{d}T$ observationally, uncertainty in cloud feedback is known to arise primarily from the sensitivities $\boldsymbol{\Theta}_i$ ([8](#)), and is in fact dominated by the sensitivity to surface temperature $\boldsymbol{\Theta}_{T_{\mathrm{sfc}}}$ (Fig. S4). By combining the four sets of observed sensitivities with the 52 sets of GCM-based controlling factor responses, we obtain a probability distribution for the predicted cloud feedback that accounts for uncertainties in the observed sensitivities and in the future environmental changes (x-axis of Fig. 2A, solid blue curve; Materials and Methods). We convolve this probability distribution with the prediction error (dashed blue curves in Fig. 2A) to yield an observationally-constrained distribution for the cloud feedback (y-axis of Fig. 2A, solid blue curve; Materials and Methods). This yields a central estimate of 0.43 W m^{-2} K^{-1} for the net global cloud feedback, with confidence intervals 0.22–0.63 W m^{-2} K^{-1} (17–83%) and 0.08–0.78 W m^{-2} K^{-1} (5–95%; Fig. 2B). This indicates a likelihood of negative global cloud feedback of less than 2.5%. The constraint constitutes a 68% reduction relative to the IPCC AR5 'very likely' range (Fig. 2B, dark red bar; note that no 'likely' range was provided), and a 35% reduction with respect to the more recent WCRP assessment range (Fig. 2B, light red bar). However, we note that a direct comparison with comprehensive assessments has to be made with caution given the different methodologies; contrary to the WCRP and IPCC assessments, our new constraint does not rely on expert judgment and focuses on a single line of evidence in the form of the most recent cloud satellite data and meteorological reanalyses.

The central estimate of the constrained cloud feedback lies remarkably close to the CMIP mean (0.42 W m^{-2} K^{-1}), supporting the validity of GCM predictions in a multi-model-mean sense. However, observations suggest substantially less positive longwave cloud feedback and more positive shortwave cloud feedback compared with GCMs (Table S1, Fig. S3C–D): the observational best estimates are 0.14 and 0.35 W m^{-2} K^{-1}, respectively, versus 0.41 and 0.01 W m^{-2} K^{-1} for the CMIP mean (but note that the observational confidence intervals encompass the CMIP mean values). In the next section, we interpret these differences by considering the contributions from individual regions and cloud regimes to global feedback.

Regional and regime-based cloud feedback constraints. The global cloud feedback is the net result of distinct cloud feedback mechanisms occurring in different parts of the world. Evidence suggests that three main processes are at play: a positive longwave feedback associated with rising cloud tops, consistent with Fixed Anvil Temperature theory (29, 30); a likely positive (but uncertain) shortwave feedback linked to decreasing tropical low cloud amount (7–11, 14–16, 31–33); and a negative shortwave feedback at high latitudes, associated with increasing cloud opacity as cloud phase changes from ice to liquid (12, 13, 34, 35). The relative importance of these processes strongly varies spatially. To illustrate this, we show maps of predicted and actual net cloud feedback, $\lambda_C(r)$, in Fig. 3. Observations and GCMs are in good agreement in terms of the broad features of the spatial cloud feedback distribution, with positive feedback across most of the tropics to middle latitudes (especially in the eastern tropical Pacific and in subtropical subsidence regions), and negative feedback in high-latitude regions. This pattern results from large and opposing longwave and shortwave changes, particularly in the tropical Pacific (Fig. S5E–F). Much of this signal is dynamically-driven,

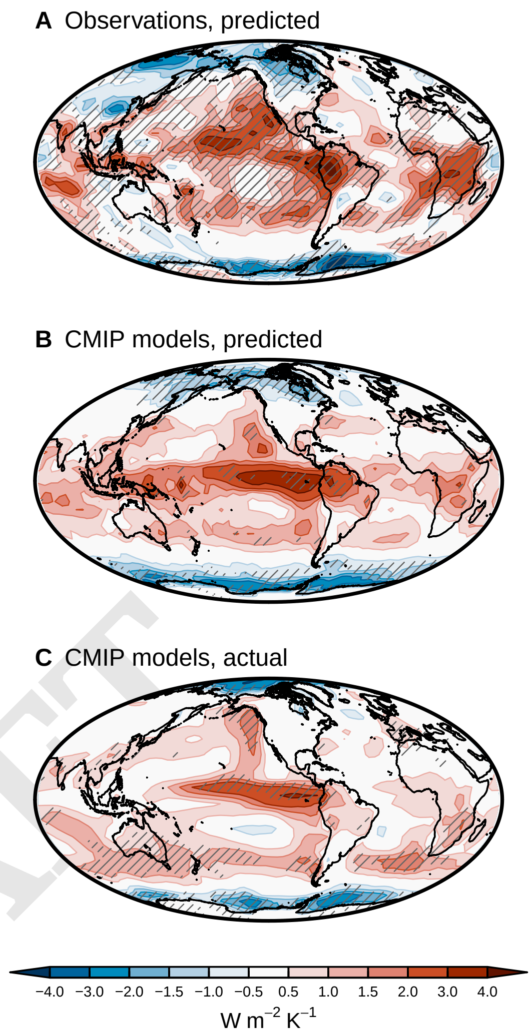

Fig. 3. (A) Predicted cloud feedback based on observed cloud responses to controlling factors (Eq. 2), calculated by averaging the sensitivities across the four reanalyses (Figs. S8–S9), and multiplying with the CMIP mean changes in controlling factors (Fig. S2A–B). (B) CMIP mean predicted cloud feedback. (C) CMIP mean actual cloud feedback. In (A), hatching denotes regions where the sign of the prediction is consistent for any choice of the set of sensitivities (based on one of four reanalyses) and controlling factor responses (based on one of 52 CMIP models). In (B) and (C), hatching denotes regions where 90% of the models agree on the sign of the feedback.

reflecting an eastward shift of the ascending branch of the Walker circulation (and associated humidity changes) whose effect is not captured by the prediction (Fig. S2C–E). We have verified that the spatial patterns of tropical longwave and shortwave feedback are very well predicted if relative humidity and vertical velocity are included as extra predictors in Eq. 2, to capture the dynamical changes (Supporting Information and Fig. S6). This dynamical signal largely cancels out for the net feedback (Fig. 3C), as expected for deep convective clouds. Dynamical signals also tend to cancel out in the global mean (36), explaining why our prediction captures the global longwave and shortwave feedbacks well (Fig. S3).

Correlation maps of actual versus predicted feedbacks indicate that our prediction method is skillful on a grid point basis for the net feedback, particularly so in the regions with the largest inter-model spread in cloud feedback (Fig. S7A, grey contours); the regional prediction is somewhat less skillful for the individual longwave and shortwave components, however, especially in those tropical areas where dynamical changes play a role (Fig. S7B–C).

We note that the spatial pattern of net cloud feedback (shortwave plus longwave) is determined primarily by the shortwave cloud-radiative sensitivity to surface temperature (Figs. S8–S9). The observed and modeled sensitivities are in excellent agreement with our physical understanding of how clouds respond to environmental changes (4, 8, 14–16, 33, 37), reinforcing confidence in our results. Further discussion of these sensitivities is given in the Supporting Information. Consistent with previous observational studies (7, 8, 10, 15, 16), the dominant T_{sfc}–mediated cloud response is partly counteracted by changes in EIS, which increases with warming across most of the tropics (38), promoting low cloud formation and thus enhanced shortwave reflection (Figs. S2B and S10). EIS also induces negative cloud-radiative responses in deep convective regions such as the Maritime Continent; this suggests EIS may serve as a proxy for factors relevant to deep convection, such as the convective available potential energy.

In addition to being calculated globally as in Fig. 2, the cloud feedback constraints can be determined for specific cloud regimes. We distinguish between low and non-low cloud regions in the tropics and extratropics, and identify these regions according to the relative magnitudes of longwave and shortwave cloud feedbacks in the GCMs (5, 39) (Fig. S11 and Table S1; Materials and Methods). By design, longwave cloud feedback is near zero in low cloud regions. The regime breakdown in Fig. S11 shows that the differences in longwave and shortwave global cloud feedbacks between models and observations arise primarily from tropical and extratropical non-low clouds (panels F–G), with a minor additional contribution from low clouds over tropical land (compare panels C and D). The observationally inferred non-low cloud longwave and shortwave feedbacks are suggestive of a decrease in high cloud area with warming, a possibility supported by observations and theory (40, 41) but thought to be underestimated by GCMs (42). Near-neutral longwave feedback is also consistent with expert judgment that the longwave radiative impacts of changing high cloud altitude and area will approximately cancel out (3).

For low clouds, our observational constraint points toward weakly positive feedback (Fig. S11B–E and Table S1), lower than prior expert assessments (3, 11) but in agreement with a more recent analysis (16). Our low cloud feedback estimate thus appears inconsistent with the large positive values simulated by some CMIP6 models, particularly in the extratropics (5). Further comparison of our results with prior low cloud feedback studies is provided in the Supporting Information.

Implications for ECS. We now consider how our revised range for the cloud feedback translates into reduced uncertainty for global warming projections. The ECS is related to effective radiative forcing F and net climate feedback λ through $\mathrm{ECS} = -F/\lambda$. To assess the implications of our cloud feedback constraint on ECS, we therefore regress $-1/\mathrm{ECS}$ against the predicted cloud feedback (Fig. 4A). The two variables are well correlated ($r = 0.71$), confirming the key role of cloud feedback for inter-model spread in ECS (1, 4, 43) ($r = 0.74$ for $-1/\mathrm{ECS}$ versus actual cloud feedback). The observational constraint translates into a probability distribution for ECS

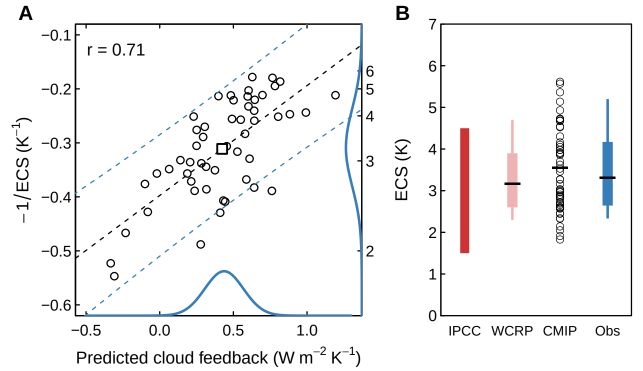

Fig. 4. (A) Negative inverse of equilibrium climate sensitivity ($-1/\mathrm{ECS}$) vs predicted cloud feedback for 52 CMIP models (circles) and the multi-model mean (square). Dashed lines represent the least-squares fit (black) and the 5–95% prediction intervals (blue). Blue curves represent probability distributions for the observational estimates (amplitudes scaled arbitrarily). Note that the y-axis on the right-hand side is in units of ECS. (B) Ranges of ECS values based on the IPCC AR5, the WCRP assessment, the CMIP models, and the observational constraint. The thick blue and red bars denote 66% confidence intervals. Black horizontal bars indicate the CMIP mean and the median (50% quantile) of the observational constraint. No central ECS estimate was provided in the IPCC AR5 report.

(Materials and Methods) with central value 3.2 K, and confidence intervals 2.6–4.2 K (17–83%; Fig. 4B, blue bar) and 2.3–5.2 K (5–95%). The former is considerably (49%) narrower than the IPCC AR5 'likely' (17–83%) range of 1.5–4.5 K, and agrees well with the slightly narrower 66% ECS range proposed by the WCRP assessment (2.6–3.9 K), which accounts for multiple lines of evidence and expert judgment rather than being based solely on cloud-radiative observations. Importantly, the constraint also confirms that ECS lower than 2 K is extremely unlikely (0.5% probability). Our 66% ECS interval is consistent with CMIP models near the middle of the range, suggesting that in a multi-model-mean sense, GCMs provide a realistic representation of climate sensitivity.

Our results demonstrate that a careful process-oriented statistical learning analysis of observed monthly variations in clouds and meteorology over a relatively short period (fewer than 20 years) can provide a powerful constraint on global and regional cloud feedbacks. Our global constraint implies that a globally positive cloud feedback is virtually certain, thus strengthening prior theoretical and modeling evidence that clouds will provide a moderate amplifying feedback on global warming through a combination of longwave and shortwave changes. This positive cloud feedback renders ECS lower than 2 K extremely unlikely, confirming scientific understanding that sustained greenhouse gas emissions will cause substantial future warming and potentially dangerous climate change.

Materials and Methods

Observational and model data. We use monthly gridded CERES-EBAF Edition 4.1 data, the state of the art in terms of satellite observations of the Earth's radiative budget (44). The CERES record is characterized by its high temporal stability (45), which makes it suitable for climate studies. We analyze top-of-atmosphere longwave and shortwave cloud-radiative effect, estimated in a manner consistent with GCMs (46). For the controlling factors, we use monthly surface and pressure level data from four reanalyses: CFSR (47), ERA5 (48), JRA-55 (49), and MERRA2 (50). The calculation of the cloud-radiative sensitivities for GCMs and observations is based on the period March 2000 to September 2019, to match the period available for CERES observations at the time of writing. For CMIP simulations, this period straddles two experiments, historical and one of the Representative Concentration Pathways (RCPs, CMIP5) or Shared Socioeconomic Pathways (SSPs, CMIP6). We therefore concatenate the historical and RCP4.5 (CMIP5) or SSP2-4.5 (CMIP6) integrations for each model, except for BCC-ESM1, where we use SSP3-7.0 since SSP2-4.5 data was unavailable. For the calculation of the controlling factor responses under climate change, cloud feedbacks and ECS (see below), we use 150 years of parallel piControl and abrupt-4xCO2 annual-mean data. We include data from 25 CMIP5 and 27 CMIP6 GCMs that provided all necessary variables and experiments at the time of writing, using only the first ensemble member for each experiment:

- CMIP5: ACCESS1.0, ACCESS1.3, BCC-CSM1.1, BCC-CSM1.1(m), BNU-ESM, CanESM2, CCSM4, CNRM-CM5, CSIRO-Mk3.6.0, GFDL-CM3, GFDL-ESM2G, GFDL-ESM2M, GISS-E2-H, GISS-E2-R, HadGEM2-ES, INMCM4, IPSL-CM5A-LR, IPSL-CM5A-MR, IPSL-CM5B-LR, MIROC5, MIROC-ESM, MPI-ESM-LR, MPI-ESM-MR, MRI-CGCM3, NorESM1-M;
- CMIP6: ACCESS-CM2, ACCESS-ESM1.5, BCC-CSM2-MR, BCC-ESM1, CESM2, CESM2-WACCM, CNRM-CM6.1, CNRM-ESM2.1, CanESM5, EC-Earth3-Veg, FGOALS-f3-L, FGOALS-g3, GFDL-CM4, GISS-E2.1-G, HadGEM3-GC31-LL, INM-CM4.8, INM-CM5.0, IPSL-CM6A-LR, MIROC-ES2L, MIROC6, MPI-ESM1.2-HR, MPI-ESM1.2-LR, MRI-ESM2.0, NESM3, NorESM2-LM, NorESM2-MM, UKESM1.0-LL.

All CERES, reanalysis and CMIP data were remapped to a common $5° \times 5°$ grid prior to analysis, using conservative remapping for radiative fluxes and bilinear interpolation for other variables.

Cloud-radiative anomalies. In Eqs. 1–2 we denote cloud-radiative anomalies in a general sense as dC. Here we introduce the specific measures of longwave (LW) and shortwave (SW) cloud-radiative anomalies used in our statistical learning analysis. We first define dR as LW and SW cloud-radiative effect anomalies (dCRE$_{\mathrm{LW}}$, dCRE$_{\mathrm{SW}}$), adjusted at each grid point r and monthly time step t for non-cloud effects (51):

$$\begin{aligned} \mathrm{d}R_{\mathrm{LW}}(r,t) &= \mathrm{dCRE}_{\mathrm{LW}}(r,t) + A^T_{\mathrm{LW}}(r,t) + A^q_{\mathrm{LW}}(r,t) + A^F_{\mathrm{LW}}(r,t), \\ \mathrm{d}R_{\mathrm{SW}}(r,t) &= \mathrm{dCRE}_{\mathrm{SW}}(r,t) + A^q_{\mathrm{SW}}(r,t) + A^a_{\mathrm{SW}}(r,t), \end{aligned} \quad [3]$$

where A denotes a LW or SW adjustment for the impact of anomalies in temperature T, water vapor q, surface albedo a, and the LW radiative forcing F_{LW}. The adjusted CRE anomalies calculated in this manner reflect the radiative impact of changes in the physical properties of clouds, excluding non-cloud influences (apart from the impact of insolation on dR_{SW}, discussed below). The calculation of these adjustments is explained in the Supporting Information.

We choose to retain the seasonal cycle in our analysis, since it contains a large signal in the controlling factors and the associated cloud-radiative responses (see additional discussion in the Supporting Information). Hence, all anomalies are defined relative to the time-mean, annual-mean climatology of the observational period. However, defining anomalies in this way means that dR_{SW} (Eq. 3) contains a large signal unrelated to physical cloud properties, due to the seasonal cycle of insolation. Instead we therefore use cloud reflectivity for the calculation of the SW cloud-radiative sensitivities:

$$\alpha_C = -(\mathrm{d}R_{\mathrm{SW}} + \overline{R_{\mathrm{SW}}})/\mathrm{SW}^{\downarrow}, \quad [4]$$

where $\overline{R_{\mathrm{SW}}}$ is the time-mean CRE$_{\mathrm{SW}}$ climatology (relative to which dR_{SW} was calculated) and SW$^{\downarrow}$ denotes monthly downward SW radiation at the top of the atmosphere. It is necessary to account for $\overline{R_{\mathrm{SW}}}$ in the calculation of α_C because the term $\overline{R_{\mathrm{SW}}}/\mathrm{SW}^{\downarrow}$ contributes to the annual cycle of α_C. We then obtain cloud reflectivity anomalies, dα_C, by subtracting the time-mean climatology of α_C at each point. Compared with dR_{SW}, dα_C is considerably less affected by insolation, but a residual effect remains because seasonal variations in solar zenith angle affect cloud albedo (52). For the calculation of the sensitivities we therefore use dR_{LW} and dα_C for the LW and SW components, respectively. The SW cloud sensitivities, initially in reflectivity units, are converted back to radiative flux units by multiplying by annual-mean insolation.

Cloud-controlling factors. We include the following five controlling factors in the ridge regression analysis (Eq. 1):

- Surface temperature (T_{sfc});
- Estimated inversion strength (EIS), a measure of lower-tropospheric stability relative to a temperature-dependent moist adiabatic lapse rate (22); over land areas, we use the simpler stability metric of Klein et al. (21), defined as the difference in potential temperature between 700 hPa and the surface;
- 700 hPa relative humidity (RH$_{700}$);
- Upper-tropospheric RH: defined as the vertically-averaged RH in the 200-hPa layer below the tropopause (53) (RH$_{\mathrm{trop}}$);
- 500 hPa vertical velocity (ω_{500}).

Only the first two, T_{sfc} and EIS, are used in the prediction model (Eq. 2); the remaining three controlling factors merely serve to ensure that the cloud-radiative sensitivities to surface temperature and stability are accurately estimated, holding relative humidity and the dynamics fixed. The motivation for using a simpler lower-tropospheric stability metric over land (instead of EIS) is that the standard EIS formula (22) is based on theoretical assumptions that only hold over sea surfaces. Further discussion of our choice of controlling factors is in the Supporting Information.

Cloud-radiative sensitivities. We use ridge regression (17) to estimate the sensitivities $\boldsymbol{\Theta}_i(r)$, which minimizes the cost function

$$\begin{aligned} J_{\mathrm{ridge}}(r,\boldsymbol{\Theta}) = &\sum_{t=1}^{n}\left(Y_t(r) - \sum_{i=1}^{M}\boldsymbol{\Theta}_i(r)\cdot \boldsymbol{X}_{i,t}(r)\right)^2 + \\ &\alpha(r)\sum_{i=1}^{M}\|\boldsymbol{\Theta}_i(r)\|^2, \end{aligned} \quad [5]$$

where $M = 5$ controlling factors and $n = 235$ months. The predictand $Y_t(r)$ is a measure of longwave (dR_{LW}, Eq. 3) or shortwave (dα_C, Eq. 4) cloud-radiative variability at time t, while $\boldsymbol{X}_{i,t}(r)$ represents a spatial map of controlling factor i at time t covering a $105°$ longitude $\times$ $55°$ latitude domain centered on the target box r. This results in a total number of predictors P = (5 factors) $\times$ (21 $\times$ 11 grid boxes) = 1155, which would lead to overfitting in MLR regressions. Next to avoiding overfitting in such contexts, ridge regression is known for its good performance in managing ill-posed problems with many collinear predictors (18, 19, 54).

The first term in Eq. 5 is the MLR least squares error which, as discussed, tends to overfit the data given large P, leading to low skill for out-of-sample predictions. Ridge regression addresses overfitting through the second l^2-norm regularization term, which penalizes large absolute values for $\boldsymbol{\Theta}$, modulated by the choice of the regularization parameter $\alpha(r)$. To approximate optimal $\alpha(r)$, we use 5-fold cross-validation (54) searching over $\alpha(r) \in [0, 10^{-12}, 3\times10^{-12}, 1\times10^{-11}, 3\times10^{-11}, ..., 1\times10^{12}, 3\times10^{12}]$ and evaluate according to the R^2 scores (coefficients of determination) across the validation sets. Statistical learning approaches of this kind are commonplace in high-dimensional machine learning regressions. We standardize each predictor variable to zero mean and unit standard deviation to ensure that all controlling factors are considered equally and so that the absolute magnitudes of the resulting sensitivities are reflective of their relative physical importance. This yields sensitivities in units of W m^{-2} σ^{-1} (Figs. S8–S9).

Our results are not sensitive to the precise choice of predictor domain size, but sensitivity calculations showed reduced skill for substantially larger or smaller domain sizes (see Supporting Information). Note that while the maximum number of predictors P is 1155 for our choice of domain, this value is smaller for locations r close to the poles, because the domains are truncated at $90°$ latitude. Furthermore, because visual inspection of the monthly α_C values reveals artifacts at high solar zenith angles, we exclude cloud reflectivity samples where the monthly-mean solar zenith angle is larger than $80°$, calculated based on a local time of 10:30AM, the equator-crossing time of the Terra satellite (44). For consistency, this criterion is applied to both observations and GCMs.

4×CO_2 responses, feedbacks, and ECS. The controlling factor responses per unit global warming ($\mathrm{d}\boldsymbol{T_{\mathrm{sfc}}}/\mathrm{d}T$ and $\mathrm{d}\mathbf{EIS}/\mathrm{d}T$ in Eq. 2) and cloud feedbacks are calculated as the slopes of Gregory regressions (55) at each point onto global-mean surface air temperature. For cloud feedbacks, we use adjusted longwave and shortwave CRE anomalies in the regressions (see above). ECS is determined as the x-intercept of a Gregory regression of net top-of-atmosphere radiative imbalance versus global-mean surface air temperature. In all cases, we use abrupt-4xCO2 annual anomalies, calculated relative to the parallel piControl 150-year climatology.

Observational constraints. The uncertainty in the cloud feedback constraint is calculated in several steps. First, we obtain a probability distribution of the observational prediction $\lambda_{C,p}$ (x-axis of Fig. 2A, solid blue curve) by combining the uncertainties due to the sensitivities, quantified by σ_Θ, with those due to the controlling factor responses, σ_X. To obtain σ_Θ, we multiply each of the four reanalysis estimates of $\boldsymbol{\Theta}_i$ with the CMIP mean controlling factor responses $\mathrm{d}\boldsymbol{X}_i/\mathrm{d}T$ (Eq. 2), take the area-weighted average, and calculate the standard deviation across these four estimates of $\lambda_{C,p}$. We follow the same procedure for σ_X, but multiplying each of the 52 estimates of $\mathrm{d}\boldsymbol{X}_i/\mathrm{d}T$ with the mean observed $\boldsymbol{\Theta}_i$. These uncertainties are then combined in quadrature, $\sigma_p = \sqrt{\sigma_\Theta^2 + \sigma_X^2}$, to yield the uncertainty for the observational prediction $\lambda_{C,p}$.

Next, the uncertainty in $\lambda_{C,p}$ is convolved with the prediction error implied by the fit of the actual cloud feedback $\lambda_{C,a}$ versus $\lambda_{C,p}$, calculated via standard least-squares regression formulae (56), whose 5–95% interval is represented by dashed blue curves in Fig. 2A. This yields a probability distribution for $\lambda_{C,a}$ on the y-axis of Fig. 2A:

$$P(\lambda_{C,a}) = \int_{-\infty}^{+\infty} P(\lambda_{C,a}|\lambda_{C,p}) P(\lambda_{C,p})\, \mathrm{d}\lambda_{C,p}, \qquad [6]$$

where the conditional probability $P(\lambda_{C,a}|\lambda_{C,p})$ represents the prediction error. $P(\lambda_{C,a})$ is calculated numerically by Monte Carlo sampling, with a sample size of 10^7, and we apply a Gaussian kernel smoother to the result with a standard deviation of 0.01 W m^{-2} K^{-1} to obtain the final probability distribution function. The constraints for global longwave and shortwave cloud feedbacks (Fig. S3), for individual cloud types and regions (Fig. S11), and for ECS (Fig. 4) are obtained via the same procedure. For ECS, the Gaussian kernel smoother uses a standard deviation of 0.1 K.

The prediction error used in the calculation of the constraints includes the effects of methodological error (e.g. due to relevant controlling factors not being accounted for, or non-linearities in the feedbacks), and sampling error (due to using a short time period for the calculation of the sensitivities). Hence, the constraints calculated via Eq. 6 account for all relevant uncertainties, namely: inaccurate observations of $\boldsymbol{\Theta}_i$; uncertain future responses $\mathrm{d}\boldsymbol{X}_i/\mathrm{d}T$; sampling error (and resulting uncertainty in the regression slopes); and methodological error.

Feedbacks by cloud type. For each GCM we classify each grid point as a low or non-low cloud region according to the relative magnitudes of the longwave and shortwave feedbacks. Following previous work (5, 39), non-low clouds are defined to occur where the ratio of the absolute magnitudes of the longwave and shortwave feedbacks exceeds $\tan(22.5°) \approx 0.42$, i.e. where the longwave feedback is relatively large. Note that the resulting values in Fig. S11 are scaled by the area fractions associated with each region and cloud type, so as to represent contributions to global-mean feedback.

ACKNOWLEDGMENTS. We thank Tim Myers and Mark Zelinka for helpful discussions. This work used the ARCHER UK National Supercomputing Service and JASMIN, the UK collaborative data analysis facility. We acknowledge the World Climate Research Programme, which, through its Working Group on Coupled Modeling, coordinated and promoted CMIP6. We thank the climate modeling groups for producing and making available their model output, the Earth System Grid Federation (ESGF) for archiving the data and providing access, and the multiple funding agencies who support CMIP6 and ESGF. P.C. was supported by an Imperial College Research Fellowship, and by NERC project NE/T006250/1. P.N. was supported by an Imperial College Research Fellowship.

1. O Boucher, et al., Clouds and Aerosols in *Climate Change 2013: The Physical Science Basis. Contribution of Working Group I to the Fifth Assessment Report of the Intergovernmental Panel on Climate Change*, eds. TF Stocker, et al. (Cambridge University Press, Cambridge, United Kingdom and New York, NY, USA), pp. 571–657 (2013).
2. MD Zelinka, DA Randall, MJ Webb, SA Klein, Clearing clouds of uncertainty. *Nat. Clim. Chang.* **7**, 674–678 (2017).
3. S Sherwood, et al., An assessment of Earth's climate sensitivity using multiple lines of evidence. *Rev. Geophys.* **58**, 1–92 (2020).
4. P Ceppi, F Brient, MD Zelinka, DL Hartmann, Cloud feedback mechanisms and their representation in global climate models. *Wiley Interdiscip. Rev. Clim. Chang.* **8**, e465 (2017).
5. MD Zelinka, et al., Causes of Higher Climate Sensitivity in CMIP6 Models. *Geophys. Res. Lett.* **47** (2020).
6. T Schneider, et al., Climate goals and computing the future of clouds. *Nat. Clim. Chang.* **7**, 3–5 (2017).
7. X Qu, A Hall, SA Klein, AM DeAngelis, Positive tropical marine low-cloud cover feedback inferred from cloud-controlling factors. *Geophys. Res. Lett.* **42**, 7767–7775 (2015).
8. TA Myers, JR Norris, Reducing the uncertainty in subtropical cloud feedback. *Geophys. Res. Lett.* **43**, 2144–2148 (2016).
9. F Brient, T Schneider, Constraints on climate sensitivity from space-based measurements of low-cloud reflection. *J. Clim.* **29**, 5821–5835 (2016).
10. DT McCoy, R Eastman, DL Hartmann, R Wood, The change in low cloud cover in a warmed climate inferred from AIRS, MODIS and ECMWF-Interim reanalysis. *J. Clim.* **30**, 15–0734 (2017).
11. SA Klein, A Hall, JR Norris, R Pincus, Low-Cloud Feedbacks from Cloud-Controlling Factors: A Review. *Surv. Geophys.* **38**, 1–23 (2017).
12. P Ceppi, DT McCoy, DL Hartmann, Observational evidence for a negative shortwave cloud feedback in middle to high latitudes. *Geophys. Res. Lett.* **43**, 1331–1339 (2016).
13. CR Terai, SA Klein, MD Zelinka, Constraining the low-cloud optical depth feedback at middle and high latitudes using satellite observations. *J. Geophys. Res. Atmospheres* **121**, 9696–9716 (2016).
14. RC Scott, et al., Observed Sensitivity of Low-Cloud Radiative Effects to Meteorological Perturbations over the Global Oceans. *J. Clim.* **33**, 7717–7734 (2020).
15. GV Cesana, AD Del Genio, Observational constraint on cloud feedbacks suggests moderate climate sensitivity. *Nat. Clim. Chang.* **11**, 213–218 (2021).
16. TA Myers, et al., Observational constraints on low cloud feedback reduce uncertainty of climate sensitivity. *Nat. Clim. Chang.* **11**, 1–7 (2021).
17. AE Hoerl, RW Kennard, Ridge Regression: Biased Estimation for Nonorthogonal Problems. *Technometrics* **12**, 55–67 (1970).
18. CF Dormann, et al., Collinearity: A review of methods to deal with it and a simulation study evaluating their performance. *Ecography* **36**, 027–046 (2013).
19. P Nowack, et al., Using machine learning to build temperature-based ozone parameterizations for climate sensitivity simulations. *Environ. Res. Lett.* **13**, 104016 (2018).
20. LA Mansfield, et al., Predicting global patterns of long-term climate change from short-term simulations using machine learning. *npj Clim. Atmospheric Sci.* **3**, 44 (2020).
21. SA Klein, DL Hartmann, The Seasonal Cycle of Low Stratiform Clouds. *J. Clim.* **6**, 1587–1606 (1993).
22. R Wood, CS Bretherton, On the Relationship between Stratiform Low Cloud Cover and Lower-Tropospheric Stability. *J. Clim.* **19**, 6425–6432 (2006).
23. KE Taylor, RJ Stouffer, GA Meehl, An Overview of CMIP5 and the Experiment Design. *Bull. Am. Meteorol. Soc.* **93**, 485–498 (2012).
24. V Eyring, et al., Overview of the Coupled Model Intercomparison Project Phase 6 (CMIP6) experimental design and organization. *Geosci. Model. Dev.* **9**, 1937–1958 (2016).
25. C Zhou, MD Zelinka, SA Klein, Impact of decadal cloud variations on the Earth's energy budget. *Nat. Geosci.* **9**, 871–874 (2016).
26. T Andrews, MJ Webb, The dependence of global cloud and lapse-rate feedbacks on the spatial structure of tropical Pacific warming. *J. Clim.* **31**, 17–0087 (2018).
27. C Proistosescu, et al., Radiative Feedbacks From Stochastic Variability in Surface Temperature and Radiative Imbalance. *Geophys. Res. Lett.* **45**, 5082–5094 (2018).
28. P Ceppi, JM Gregory, A refined model for the Earth's global energy balance. *Clim. Dyn.* **53**, 4781–4797 (2019).
29. DL Hartmann, K Larson, An important constraint on tropical cloud–climate feedback. *Geophys. Res. Lett.* **29**, 1951 (2002).
30. MD Zelinka, DL Hartmann, Why is longwave cloud feedback positive? *J. Geophys. Res.* **115**, D16117 (2010).
31. S Bony, JL Dufresne, Marine boundary layer clouds at the heart of tropical cloud feedback uncertainties in climate models. *Geophys. Res. Lett.* **32**, L20806 (2005).
32. M Rieck, L Nuijens, B Stevens, Marine Boundary Layer Cloud Feedbacks in a Constant Relative Humidity Atmosphere. *J. Atmospheric Sci.* **69**, 2538–2550 (2012).
33. CS Bretherton, Insights into low-latitude cloud feedbacks from high-resolution models. *Philos. transactions. Ser. A, Math. Phys. Eng. Sci.* **373**, 3354–3360 (2015).
34. MD Zelinka, SA Klein, DL Hartmann, Computing and Partitioning Cloud Feedbacks Using Cloud Property Histograms. Part II: Attribution to Changes in Cloud Amount, Altitude, and Optical Depth. *J. Clim.* **25**, 3736–3754 (2012).
35. DT McCoy, DL Hartmann, MD Zelinka, P Ceppi, DP Grosvenor, Mixed-phase cloud physics and Southern Ocean cloud feedback in climate models. *J. Geophys. Res. Atmospheres* **120**, 9539–9554 (2015).
36. MP Byrne, T Schneider, Atmospheric Dynamics Feedback: Concept, Simulations, and Climate Implications. *J. Clim.* **31**, 3249–3264 (2018).
37. TA Myers, JR Norris, Observational Evidence That Enhanced Subsidence Reduces Subtropical Marine Boundary Layer Cloudiness. *J. Clim.* **26**, 7507–7524 (2013).
38. X Qu, A Hall, SA Klein, PM Caldwell, The strength of the tropical inversion and its response

to climate change in 18 CMIP5 models. *Clim. Dyn.* **45**, 375–396 (2015).
39. MJ Webb, et al., On the contribution of local feedback mechanisms to the range of climate sensitivity in two GCM ensembles. *Clim. Dyn.* **27**, 17–38 (2006).
40. S Bony, et al., Thermodynamic control of anvil cloud amount. *Proc. Natl. Acad. Sci. United States Am.* **113**, 8927–32 (2016).
41. M Saint-Lu, S Bony, J Dufresne, Observational evidence for a stability Iris effect in the Tropics. *Geophys. Res. Lett.* **47** (2020).
42. T Vaillant de Guélis, et al., Space lidar observations constrain longwave cloud feedback. *Sci. Reports* **8**, 16570 (2018).
43. PM Caldwell, MD Zelinka, KE Taylor, K Marvel, Quantifying the Sources of Intermodel Spread in Equilibrium Climate Sensitivity. *J. Clim.* **29**, 513–524 (2016).
44. NG Loeb, et al., Clouds and the Earth's Radiant Energy System (CERES) Energy Balanced and Filled (EBAF) Top-of-Atmosphere (TOA) Edition-4.0 Data Product. *J. Clim.* **31**, 895–918 (2018).
45. N Loeb, N Manalo-Smith, W Su, M Shankar, S Thomas, CERES Top-of-Atmosphere Earth Radiation Budget Climate Data Record: Accounting for in-Orbit Changes in Instrument Calibration. *Remote. Sens.* **8**, 182 (2016).
46. NG Loeb, et al., Toward a Consistent Definition between Satellite and Model Clear-Sky Radiative Fluxes. *J. Clim.* **33**, 61–75 (2020).
47. S Saha, et al., The NCEP climate forecast system reanalysis. *Bull. Am. Meteorol. Soc.* **91**, 1015–1058 (2010).
48. H Hersbach, et al., Global reanalysis: goodbye ERA-Interim, hello ERA5. *ECMWF Newsl.* **159**, 17–24 (2019).
49. S Kobayashi, et al., The JRA-55 reanalysis: General specifications and basic characteristics. *J. Meteorol. Soc. Jpn.* **93**, 5–48 (2015).
50. R Gelaro, et al., The Modern-Era Retrospective Analysis for Research and Applications, Version 2 (MERRA-2). *J. Clim.* **30**, 5419–5454 (2017).
51. BJ Soden, et al., Quantifying Climate Feedbacks Using Radiative Kernels. *J. Clim.* **21**, 3504–3520 (2008).
52. DL Hartmann, *Global Physical Climatology.* (Academic Press), p. 411 (1994).
53. T Reichler, M Dameris, R Sausen, Determining the tropopause height from gridded data. *Geophys. Res. Lett.* **30**, 2042 (2003).
54. CM Bishop, *Pattern Recognition and Machine Learning.* (Springer, New York), pp. 1–738 (2006).
55. JM Gregory, et al., A new method for diagnosing radiative forcing and climate sensitivity. *Geophys. Res. Lett.* **31**, L03205 (2004).
56. DS Wilks, *Statistical Methods in the Atmospheric Sciences.* (Academic Press), p. 648 (2006).